Quantum-mechanical calculations of charge transfer in collisions of O^{3+} with He

Y. Wu,[1] Y. Y. Qi,[1,2] S. Y. Zou,[1] J. G. Wang,[1] Y. Li,[3] R. J. Buenker,[3] and P. C. Stancil[4]
[1]*Institute of Applied Physics and Computational Mathematics, P.O. Box 8009, Beijing 100088, China*
[2]*School of Electrical Engineering, Jiaxing University, Jiaxing 314001, China*
[3]*Fachbereich C-Mathematik und Naturwissenschaften, Bergische Universität Wuppertal, D-42097 Wuppertal, Germany*
[4]*Department of Physics and Astronomy and the Center for Simulational Physics, University of Georgia, Athens, Georgia 30602-2451, USA*
(Received 27 April 2009; published 17 June 2009)

Charge transfer due to collisions of ground-state $O^{3+}(2s^2 2p\ ^2P)$ ions with He is investigated using the quantum-mechanical molecular-orbital close-coupling (QMOCC) method. The *ab initio* adiabatic potentials and radial couplings utilized in the QMOCC calculations are obtained from the multireference single- and double-excitation configuration interaction approach. State-selective and total charge-transfer cross sections are calculated for collision energies from 0.01 eV/u to 1 keV/u. Comparison with existing data reveals that the present QMOCC calculations are in good harmony with the measured total single-electron charge-transfer cross sections. Excellent agreement with the available experimental data is also found for state-selective cross sections at the measured energy region.

DOI: 10.1103/PhysRevA.79.062711 PACS number(s): 34.50.−s, 34.10.+x

I. INTRODUCTION

Charge transfer in collisions of highly charged ions with neutral atoms and molecules has attracted much attention. This interest stems not only from fundamental aspects but also from the importance of electron-capture processes in astrophysics and plasma physics. Charge transfer provides a recombination mechanism for multiply charged ions in x-ray-ionized astronomical environments which may have sparse electron abundances [1]. In the divertor region of a tokamak fusion device, charge exchange of impurity ions with neutral atoms and molecules plays an important role in the ionization balance and the production of radiative energy loss leading to cooling [2,3]. In the core of the plasma, charge exchange spectra produced by neutral beam injection are also an important method for diagnosing the populations of impurities. Recently, it has been found that ion-atom or -molecule charge-transfer processes are of particular significance to euv and x-ray emission from comets, planetary atmospheres, and the heliosphere. Soft x-ray emission has been observed from many comets including comet Hale-Bopp [4] and comet Hyakutake [5,6]. It is believed that the x-ray emission is due to charge transfer of heavy solar wind ions (such as O^{q+}, C^{q+}, Ne^{q+}, and Si^{q+}, $q=3-8$) with cometary neutral species such as H, O, H_2, H_2O, OH, and CO [7,8]. Indeed, analysis of x-ray spectra of eight comets observed by the Chandra X-ray Observatory [9] confirmed that such charge-transfer processes are responsible for the observed x-ray emission. In a similar way, x-ray emissions from the Jovian aurora are thought to be driven by charge transfer in collisions of multiply charged oxygen and sulfur ions with atmospheric neutrals such as H, He, and H_2 [10,11]. In order to model and understand the behavior of these environments, it is necessary to obtain total and especially state-selective capture cross sections.

Due to the importance in astrophysics and plasma physics, collisions of low-energy O^{3+} with He have been studied extensively both by experiment and theory. Recently, several groups have reported their work on this process [12–14]. Bangsgaard *et al.* [12] used the translational energy-gain spectroscopy technique to measure the total and state-selective single-electron capture (SEC) cross sections for a few projectile energies between 250 and 1500 eV. Ishii *et al.* [13] measured total single- and double-charge exchange cross section for a broader range of collision energies from 3 to 5400 eV, and they also estimated the single- and double-charge exchange cross sections using the classical over-barrier (COB) and multichannel Landau-Zener (MCLZ) methods. However, large discrepancies exist between their measurements and calculations. More recently, Kamber *et al.* [14] also used the translational energy-gain spectroscopy technique to measure the total single-electron capture cross sections for projectile energies from 300 to 1500 eV and their results agree well with the measurements of Bangsgaard *et al.* and Ishii *et al.* Besides the COB and MCLZ calculations of Ishii *et al.* [13], Butler and Dalgarno [15] have performed two-channel Landau-Zener calculation at thermal energies.

In the present work, the charge-transfer process due to collisions of ground-state $O^{3+}(2s^2 2p\ ^2P^o)$ ions with helium is investigated by using the quantum-mechanical MOCC method. The adiabatic potential curves and radial coupling matrix elements are calculated with an *ab initio* multireference configuration interaction (MRD-CI) package [16–18]. Total and state-selective cross sections are obtained and compared with the available theoretical and experimental data. Section II describes the electronic structure calculation of $[OHe]^{3+}$, while Sec. III introduces the scattering calculation approach briefly. Section IV presents the adiabatic and diabatic potentials and radial coupling matrix elements as well as the results of the scattering calculations, while Sec. V briefly gives a summary of the work. Atomic units are used throughout unless otherwise noted.

II. ELECTRONIC STRUCTURE CALCULATION

In the present study, an *ab initio* configuration interaction calculation (CI) is carried out for seven $^2\Sigma^+$ electronic states

TABLE I. Comparison of asymptotic energies of the $[OHe]^{3+}$ system between the present MRDCI calculation and the corresponding experimental data [21]; ΔE is the absolute error between the calculated and experimental data.

Molecular states	MRDCI results (eV)	Experimental values (eV) [21]	ΔE (eV)
$1\ ^2\Sigma^+[O^{2+}(2s^22p^2\ ^1D)+He^+(1s\ ^2S)]$	2.5434	2.5136	0.0298
$2\ ^2\Sigma^+[O^{2+}(2s^22p^2\ ^1S)+He^+(1s\ ^2S)]$	5.4087	5.3544	0.0543
$3\ ^2\Sigma^+[O^{2+}(2s2p^3\ ^3P^o)+He^+(1s\ ^2S)]$	17.6373	17.6532	0.0159
$4\ ^2\Sigma^+[O^+(2s^22p^3\ ^2P^o)+He^{2+}]$	24.4645	24.3140	0.1505
$5\ ^2\Sigma^+[O^{2+}(2s2p^3\ ^1P^o)+He^+(1s\ ^2S)]$	26.1609	26.0939	0.0670
$6\ ^2\Sigma^+[O^{3+}(2s^22p\ ^2P^o)+He(1s^2\ ^1S)]$	30.3597	30.3800	0.0203
$7\ ^2\Sigma^+[O^{2+}(2s^22p3s\ ^3P^o)+He^+(1s\ ^2S)]$	33.1247	33.1666	0.0419
$1\ ^2\Pi[O^{2+}(2s^22p^2\ ^3P)+He^+(1s\ ^2S)]$	0.0	0.02577	0.0258
$2\ ^2\Pi[O^{2+}(2s^22p^2\ ^1D)+He^+(1s\ ^2S)]$	2.54635	2.51356	0.0328
$3\ ^2\Pi[O^{2+}(2s2p^3\ ^3D^o)+He^+(1s\ ^2S)]$	14.83085	14.8832	0.0524
$4\ ^2\Pi[O^{2+}(2s2p^3\ ^3P^o)+He^+(1s\ ^2S)]$	17.63092	17.6532	0.0223
$5\ ^2\Pi[O^+(2s^22p^3\ ^2D^o)+He^{2+}]$	22.75189	22.6218	0.1301
$6\ ^2\Pi[O^{2+}(2s2p^3\ ^1D^o)+He^+(1s\ ^2S)]$	23.22529	23.19174	0.0336
$7\ ^2\Pi[O^+(2s^22p^3\ ^2P^o)+He^{2+}]$	24.46294	24.314	0.1489
$8\ ^2\Pi[O^{2+}(2s2p^3\ ^1P^o)+He^+(1s\ ^2S)]$	26.16208	26.09394	0.0681
$9\ ^2\Pi[O^{3+}(2s^22p\ ^2P^o)+He(1s^2\ ^1S)]$	30.34771	30.38001	0.0323
$10\ ^2\Pi[O^{2+}(2s^22p3s\ ^3P^o)+He^+(1s\ ^2S)]$	33.12118	33.1666	0.0454

in A_1 symmetry and ten electronic $^2\Pi$ states in B_1 symmetry of $[OHe]^{3+}$ system by using the MRD-CI package [16–18]. A $(6s,2p,1d)$ contracted to $[3s,2p,1d]$ basis set [19] is employed for helium, and a $(21s,6p,3d,2f)$ contracted to $[5s,4p,3d,2f]$ basis set [20] is employed for oxygen. A diffuse $(2s2p2d)$ basis set centered on the O atom is employed to describe its Rydberg states, while a diffuse $(1s1p1d)$ set is used for the He atom. All the above Rydberg basis sets are optimized based on measured atomic energy levels. A threshold of 2×10^{-8} hartrees is used to select the configuration wave functions for $[OHe]^{3+}$ for internuclear distances from 1.5 to 40 a_0. The total number of selected configuration functions is dependent on the symmetries of the electronic states considered and generally are less than 35 000. The energy lowering contribution from the unselected configuration functions is considered by employing an extrapolation procedure [16,17]. As shown in Table I, the errors in the calculated energies are less than 0.15 eV in the asymptotic region, which is adequate for most of the scattering calculations [22]. The resulting highly correlated electronic wave functions are then employed to calculate the radial couplings among the separate $^2\Sigma^+$ states or $^2\Pi$ states by using finite differentiation [23].

III. SCATTERING METHOD

The quantum-mechanical molecular-orbital close-coupling (QMOCC) method, which we only briefly discuss here, has been described thoroughly in the literature (e.g., Kimura and Lane [24], Zygelman *et al.* [25], and Wang *et al.* [26]). It involves solving a coupled set of second-order differential equations using the log-derivative method of Johnson [27]. In the adiabatic representation, transitions between channels are driven by radial and rotational matrix elements of the vector potential $\underline{A}(\vec{R})$, where $\vec{R}$ is the internuclear distance vector. Since the adiabatic description contains first-order derivatives, it is numerically convenient to make a unitary transformation [25,28,29], which is dependent on the radial portion of $\underline{A}(\vec{R})$, to a diabatic representation

$$\underline{U}(R) = \underline{W}(R)[\underline{V}(R) - \underline{P}(R)]\underline{W}^{-1}(R), \tag{1}$$

where $\underline{U}(R)$ is the diabatic potential matrix, $\underline{V}(R)$ is the diagonal adiabatic potential, $\underline{W}(R)$ is a unitary transformation matrix, and $\underline{P}(R)$ is the rotational matrix of the vector potential $\underline{A}(\vec{R})$ [26,30,31]. In this work, the rotational couplings are neglected, since radial coupling is expected to be the dominant mechanism for charge transfer in the calculated energy region [26,32,33]. With the diabatic potentials and couplings, the coupled set of second-order differential equations is solved to obtain the K matrix from the scattering amplitude after a partial-wave decomposition (see, e.g., Zygelman *et al.* [25]). The electron capture cross section is then given by

$$\sigma_{\alpha\to\beta} = \frac{\pi g_\alpha}{k_\alpha^2}\sum_J (2J+1)|(S_J)_{\alpha\beta}|^2, \tag{2}$$

where the S matrix is defined as

$$\underline{S}_J = [\underline{I} + i\underline{K}_J]^{-1}[\underline{I} - i\underline{K}_J]. \tag{3}$$

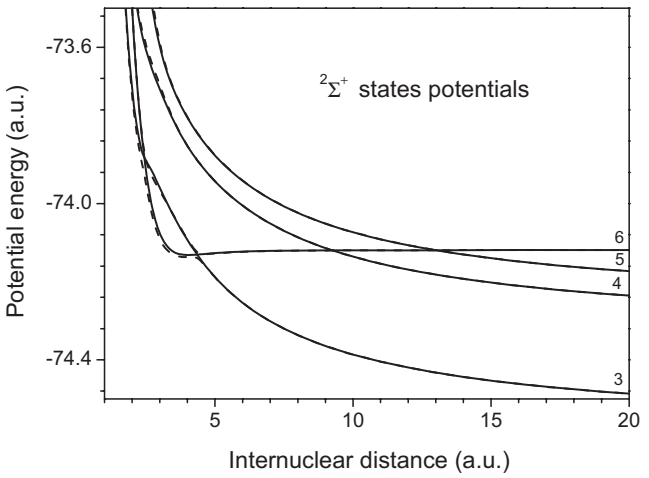

FIG. 1. Adiabatic (solid lines) and diabatic potentials (dashed lines) of $[OHe]^{3+}$ $^2\Sigma^+$ states as a function of internuclear distance. The curves denote $O^{2+}(2s2p^3\ ^3P^o)+He^+(1s\ ^2S)(3\ ^2\Sigma^+)$, $O^+(2s^22p^3\ ^2P^o)+He^{2+}(4\ ^2\Sigma^+)$, $O^{2+}(2s2p^3\ ^1P^o)+He^+$ $(1s\ ^2S)$ $(5\ ^2\Sigma^+)$, and $O^{3+}(2s^22p\ ^2P^o)+He(1s^2\ ^1S)$ $(6\ ^2\Sigma^+)$ states from bottom to top for both adiabatic and diabatic states.

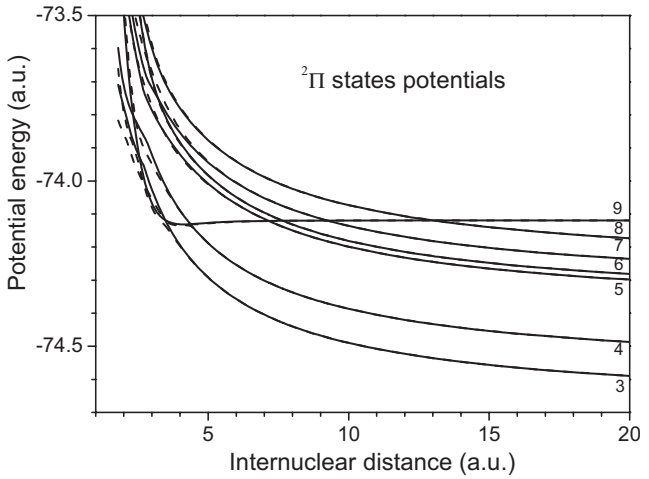

FIG. 2. Adiabatic (solid lines) and diabatic potentials (dashed lines) of $[OHe]^{3+}$ $^2\Pi$ states as a function of internuclear distance. The curves denote $O^{2+}(2s2p^3\ ^3D^o)+He^+$ $(1s\ ^2S)$ $(3\ ^2\Pi)$, $O^{2+}(2s2p^3\ ^3P^o)+He^+(1s\ ^2S)$ $(4\ ^2\Pi)$, $O^+(2s^22p^{3\,2}D^o)+He^{2+}(5^2\Pi)$, $O^{2+}(2s2p^3\ ^1D^o)+He^+$ $(1s\ ^2S)$ $(6\ ^2\Pi)$, $O^+(2s^22p^3\ ^2P^o)+He^{2+}(7\ ^2\Pi)$, $O^{2+}(2s2p^3\ ^1P^o)+He^+$ $(1s\ ^2S)$ $(8\ ^2\Pi)$, and $O^{3+}(2s^22p\ ^2P^o)$ $+He(1s^2\ ^1S)$ $(9\ ^2\Pi)$ states from bottom to top for both adiabatic and diabatic states.

$\underline{I}$ is the identity matrix, k_α denotes the wave number for center-of-mass motion of the initial ion-atom channel, and g_α is an approach probability factor of the initial channel α. Electron translation factors (ETF's) [24] are not included in the current calculations, since the influence of ETF's is only expected to be important when the incident energy $E>1$ keV/u [26,34,35]. The method described above is carried out for each partial wave J until a converged cross section is attained.

IV. RESULTS AND DISCUSSIONS

Since the symmetries of the entrance channels of $O^{3+}(2s^22p\ ^2P^o)+He(1s^2\ ^1S)$ are exclusively $^2\Sigma^+$ and $^2\Pi$, we only treat exit channels of these symmetries. Seven $^2\Sigma^+$ and ten $^2\Pi$ electronic states are computed with the MRDCI approach, in which the 6 $^2\Sigma^+$ and 9 $^2\Pi$ correspond to the incident channel. As shown in Table I, the energy intervals between 2 $^2\Sigma^+$ and 3 $^2\Sigma^+$ states and between 2 $^2\Pi$ and 3 $^2\Pi$ states are as large as $\sim$12.5 eV in the asymptotic region, while 7 $^2\Sigma^+$ and 10 $^2\Pi$ states are endothermic channels, so that these states including 1 $^2\Sigma^+$, 2 $^2\Sigma^+$, and 7 $^2\Sigma^+$ and 1 $^2\Pi$, 2 $^2\Pi$, and 10 $^2\Pi$ should not be important for charge-transfer processes in the concerned energy region. Therefore, four $^2\Sigma^+$ channels (3, 4, 5, and 6) and seven $^2\Pi$ channels (3–9) are included in our QMOCC calculations.

A. Potentials and radial couplings

Figure 1 displays the adiabatic and diabatic potentials of $[OHe]^{3+}$ $(^2\Sigma^+)$, as a function of internuclear distance, considered in the scattering calculations. Strong avoided crossings appear at about 13, 9.3, 4.4, and 2.4 a_0, which are responsible for driving the transitions between $^2\Sigma^+$ channels. The diabatic potentials cross at those avoided crossing points as expected. The adiabatic and diabatic potentials of $[OHe]^{3+}$ $(^2\Pi)$ are plotted in Fig. 2. Strong avoided crossings appear around 13, 9.3, 7.7, 7.2, 4.4, 2.7, and 2.4 a_0 in the adiabatic potentials and the resulting diabatic potentials cross at these positions.

In Fig. 3, the nonadiabatic radial coupling matrix elements between the adjacent states are presented for the $^2\Sigma^+$ and $^2\Pi$ states, respectively. The positions for each peak are consistent with the positions of the avoided crossings as shown in Figs. 1 and 2. It can be found that the inner radial couplings around 4.4 and 2.4 a_0 for $^2\Sigma^+$ states and around 4.4, 2.7, and 2.4 a_0 for $^2\Pi$ states are much broader and smaller compared with the sharp outer radial couplings, and these avoided crossings are expected to play dominant roles in the charge-transfer processes. To the best of our knowledge, no adiabatic potentials or radial coupling data are available in the literature for $[OHe]^{3+}$ system. The positions and the adiabatic energy splittings for these avoided crossings are given in Table II. For the bigger avoided crossing distance $R_x>7$ a_0, the energy separations are too small to be so accurate as the cases for $R_x<7$ a_0 due to the computational accuracies in the MRDCI method. But they can be treated as the diabatic processes and their contributions to the charge-transfer cross sections are not important.

Figure 4 plots the diabatic radial couplings of $[OHe]^{3+}$ $(^2\Sigma^+)$ as a function of internuclear distance. Except for short internuclear distances $(R<2\ a_0)$, the couplings vary smoothly with R. Approaching the united-atom limit, some short-range avoided crossings are present and contribute to the erratic behavior. The diabatic radial couplings for the $(^2\Pi)$ states are plotted in Fig. 5.

B. Total and state-selective cross sections

Using the QMOCC method, total and state-selective electron capture cross sections in collisions of O^{3+} with He are

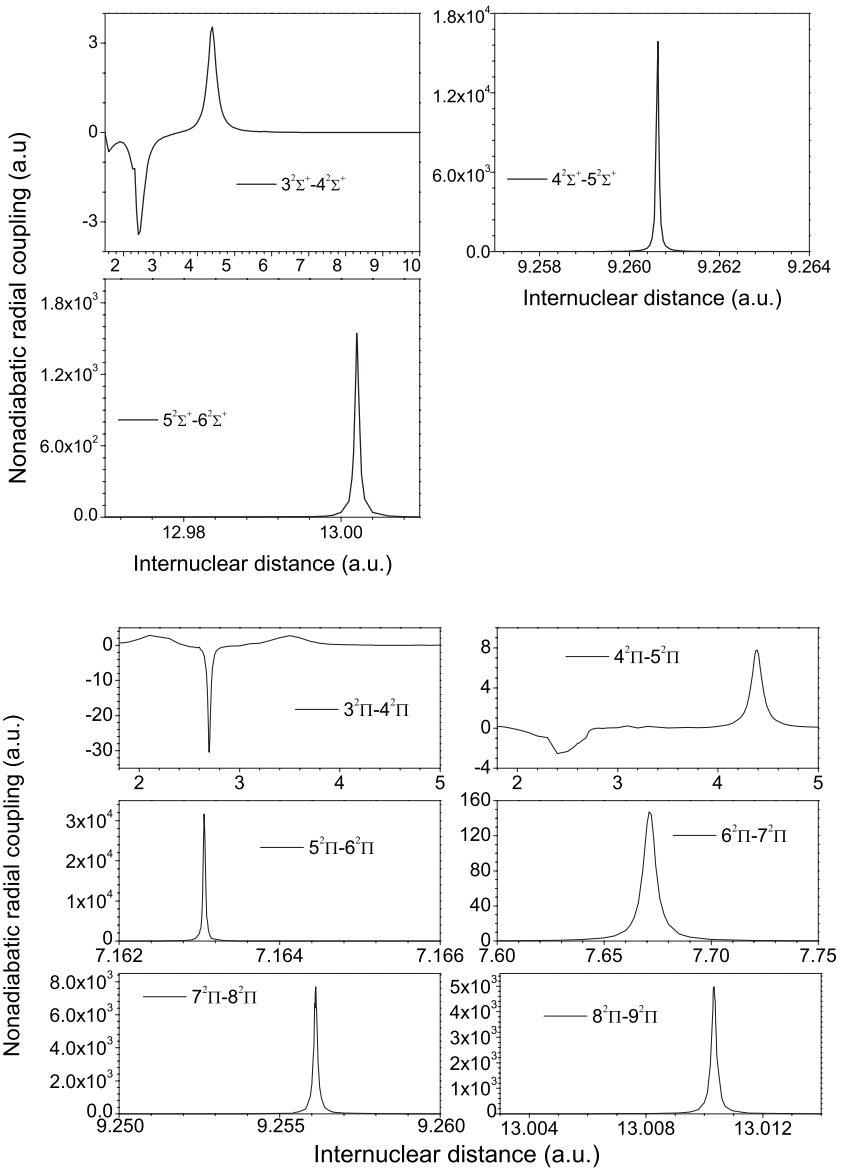

FIG. 3. Nonadiabatic radial couplings of $[OHe]^{3+}$ as a function of internuclear distance. Upper figures: couplings between $^2\Sigma^+$ states; lower figures: couplings between $^2\Pi$ states. Note that different height and width scales are used for the various plots.

calculated from 0.01 eV/u to 1 keV/u. The total cross sections are compared with available experimental and theoretical results as shown in Fig. 6. SEC dominates the charge-transfer process in the considered energy region, but the SEC cross section decreases gradually as the collision energy increases. There are two slight humps at collision energies of 1 and 10 eV/u, which also appear in the measurements of Ishii *et al.* [13]. From about 10 to 100 eV/u, the current QMOCC calculations agree with all the measured data within experimental errors, but obvious discrepancies exist between the

TABLE II. Avoided crossing distances and energy separations for the adiabatic states of $[OHe]^{3+}$ (adiabatic labels).

Molecular states	R_x (units of a_0)	ΔU (eV)	Molecular states	R_x (units of a_0)	ΔU (eV)
$3\ ^2\Sigma^+-4\ ^2\Sigma^+$	2.40	0.0640	$3\ ^2\Pi-4\Pi$	2.70	0.0024
$3\ ^2\Sigma^+-4\ ^2\Sigma^+$	4.40	0.0149	$4\ ^2\Pi-5\Pi$	2.40	0.1045
$4\ ^2\Sigma^+-5\ ^2\Sigma^+$	9.26	6.46×10^{-7}	$4\ ^2\Pi-5\Pi$	4.39	0.00689
$5\ ^2\Sigma^+-6\ ^2\Sigma^+$	13.00	3.80×10^{-6}	$5\ ^2\Pi-6\Pi$	7.16	7.22×10^{-7}
			$6\ ^2\Pi-7\Pi$	7.671	1.156×10^{-4}
			$7\ ^2\Pi-8\Pi$	9.26	1.61×10^{-6}
			$8\ ^2\Pi-9\Pi$	13.01	1.226×10^{-6}

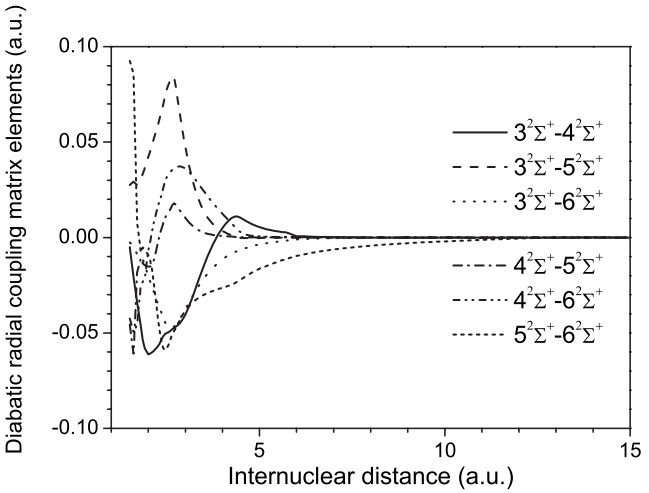

FIG. 4. Diabatic radial couplings of $[OHe]^{3+}$ $^2\Sigma^+$ states as a function of internuclear distance. Solid line, 3 $^2\Sigma^+-4$ $^2\Sigma^+$; dashed line, 3 $^2\Sigma^+-5$ $^2\Sigma^+$; dotted line, 3 $^2\Sigma^+-6$ $^2\Sigma^+$; dash-dotted line, 4 $^2\Sigma^+-5$ $^2\Sigma^+$; dash-dot dotted line, 4 $^2\Sigma^+-6$ $^2\Sigma^+$; short-dashed line, 5 $^2\Sigma^+-6$ $^2\Sigma^+$.

MCLZ calculations of Ishii *et al.* [13] and the measurements for collision energies greater than 20 eV/u, despite the good agreement at lower energies. The COB approximation [13] overestimates the magnitude and clearly has the wrong energy dependence. For lower energies ($E<5$ eV/u), the present SEC cross sections are about 50%–100% larger than the experimental results of Ishii *et al.* [13]. This difference may be caused by angular scattering effects [12,36], which lead to the underestimation of the absolute cross sections for low collision energies in the measurements. At collision energies greater than 300 eV/u, the present calculation underestimates the measurement of Ishii *et al.* [13]. This may result from the omission of the lowest four channels, 1 $^2\Sigma^+$, 2 $^2\Sigma^+$, 3 $^2\Pi$, and 4 $^2\Pi$, which may contribute to the total cross sections at high collision energies, while the endothermic channels $[O^{2+}(2s^22p3s\ ^3P^o)+He^+\ (1s\ ^2S)\ (7\ ^2\Sigma^+)$ and $O^{2+}(2s^22p3s\ ^3P^o)+He^+\ (1s\ ^2S)(10\ ^2\Pi)]$ likely become important at much higher energies.

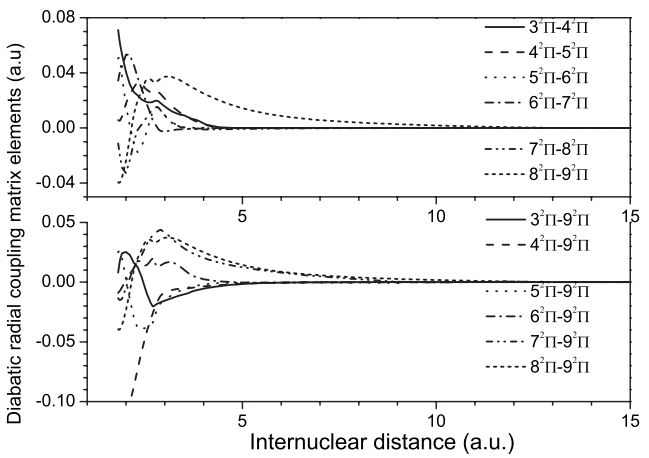

FIG. 5. Diabatic radial couplings of $[OHe]^{3+}$ ($^2\Pi$) as a function of internuclear distance. The upper figure: solid line, 3 $^2\Pi-4$ $^2\Pi$; dashed line, 4 $^2\Pi-5$ $^2\Pi$; dotted line, 5 $^2\Pi-6$ $^2\Pi$; dash-dotted line, 6 $^2\Pi-7$ $^2\Pi$; dash-dot dotted line, 7 $^2\Pi-8$ $^2\Pi$; short-dashed line, 8 $^2\Pi-9$ $^2\Pi$; The lower figure: solid line, 3 $^2\Pi-9$ $^2\Pi$; dashed line, 4 $^2\Pi-9$ $^2\Pi$; dotted line, 5 $^2\Pi-9$ $^2\Pi$; dash-dotted line, 6 $^2\Pi-9$ $^2\Pi$; dash-dot dotted line, 7 $^2\Pi-9$ $^2\Pi$; short-dashed line, 8 $^2\Pi-9$ $^2\Pi$.

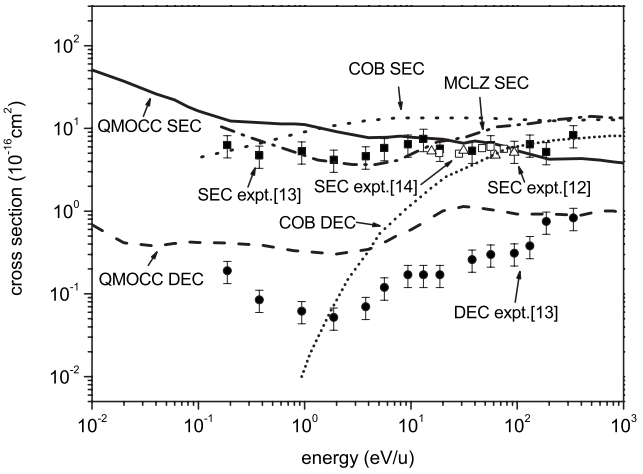

FIG. 6. Total SEC and DEC cross sections for O^{3+}+He collisions. Calculations: current QMOCC SEC (solid line) and DEC (dashed line), MCLZ SEC [13] (dash-dotted line), COB [13] SEC (dotted line), and DEC (short dotted line). SEC experiments: Ref. [12] (unfilled triangles), Ref. [13] (filled squares), and Ref. [14] (unfilled squares). DEC experiments: Ref. [13] (filled circles).

For the double-electron capture (DEC) process, there exists some discrepancies between the current results and the measurements of Ishii *et al.* [13]. The new QMOCC calculations overestimate the cross section by as much as a factor of 3 for $E<100$ eV/u, which may be partly caused by the computational precision in the potential and radial coupling calculations. It can be observed from Table I that there are errors of about 0.15 eV in the asymptotic energies for the double-electron capture channels. To check the effects of the computational precision, we reduced the asymptotic energies of the DEC channels by about 0.1 eV in agreement with the experimental values and found that the change in the single-electron capture cross sections can be neglected, but for the DEC process, a large change appears for incident energies $E<10$ eV/u. This reveals that the present computational precision of MRDCI may affect the calculations for the weak DEC process at very low incident energies. Meanwhile, this discrepancy may also be due to angular scattering effects [12,36] in the experiment. Another possibility is that the DEC process is too weak to be measured accurately. As the collision energy increases, the DEC cross section increases; when $E>100$ eV/u, the DEC cross section approaches 10^{-16} cm^2 and our results fall within the experimental errors.

State-selective single-electron and double-electron capture cross sections are shown in Fig. 7. It should be noted that both the SEC and DEC processes involve two-electron and two-center interactions. For SEC, in addition to the capture of the electron from He to the oxygen ion, the $2s$ electron in the oxygen ion is excited into $2p$ creating the core-excited configuration $2s2p^3$. The two-electron interactions increase the difficulties of MRDCI calculations. In the low-

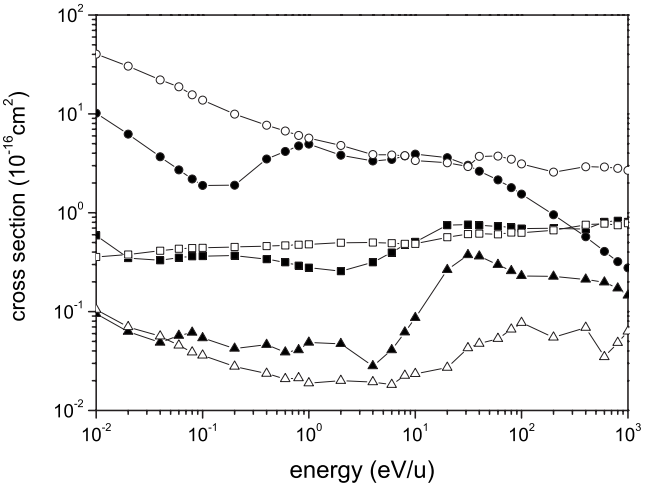

FIG. 7. State-selective QMOCC SEC and DEC cross sections for O^{3+}+He. Solid line with filled circles: SEC to $[O^{2+}(2s2p^3\ ^3D^o)+He^+(1s\ ^2S)]$; solid line with unfilled circles: SEC to $[O^{2+}(2s2p^3\ ^3P^o)+He^+(1s\ ^2S)]$; solid line with filled squares: DEC to $[O^+(2s^22p^3\ ^2P^o)+He^{2+}]$; solid line with unfilled squares: SEC to $[O^{2+}(2s2p^3\ ^1P^o)+He^+(1s\ ^2S)]$; solid line with filled triangles: DEC to $[O^+(2s^22p^3\ ^2D^o)+He^{2+}]$; solid line with unfilled triangles: SEC to $[O^{2+}(2s2p^3\ ^1D^o)+He^+(1s\ ^2S)]$.

energy region ($E<20$ eV/u), captures to the channels $O^{2+}(2s2p^3\ ^3D^o)+He^+$ $(1s\ ^2S)$ and $O^{2+}(2s2p^3\ ^3P^o)+He^+$ $(1s\ ^2S)$ dominate the charge-transfer process, and the cross sections for capture to the other four channels $O^{2+}(2s2p^3\ ^1D^o)+He^+$ $(1s\ ^2S)$, $O^{2+}(2s2p^3\ ^1P^o)+He^+$ $(1s\ ^2S)$, $O^+(2s^22p^3\ ^2D^o)+He^{2+}$ and $O^+(2s^22p^3\ ^2P^o)+He^{2+}$ are less than 10% of the two dominant channels. This results from the strong couplings between $3\ ^2\Pi-4\ ^2\Pi$, $4\ ^2\Pi-5\ ^2\Pi$, and $3\ ^2\Sigma^+-4\ ^2\Sigma^+$ at the avoided crossing positions ~2.7, ~2.4, and 4.4 a_0, respectively. There are larger and narrower radial couplings at ~9.26 and 1.3 a_0 for the $^2\Sigma^+$ states and at ~7.2, 7.6, 9.26, and 1.3 a_0 for the $^2\Pi$ states, as shown in Fig. 3; most of these interactions can be treated as diabatic so that the corresponding cross sections are small. With increasing energy, the cross section for capture to $O^{2+}(2s2p^3\ ^3P^o)+He^+$ $(1s\ ^2S)$ drops rapidly while capture to $O^{2+}(2s2p^3\ ^3D^o)+He^+$ $(1s\ ^2S)$ remains constant. It is interesting that there are two humps at about 1 and 10 eV/u for $O^{2+}(2s2p^3\ ^3P^o)+He^+$ $(1s\ ^2S)$, which are due to the avoided crossing at ~2.7 a_0 for $O^{2+}(2s2p^3\ ^3D^o)+He^+$ $(1s\ ^2S)$ lying between the two avoided crossings at ~2.4 and ~4.4 a_0 for $O^{2+}(2s2p^3\ ^3P^o)+He^+$ $(1s\ ^2S)$. The cross sections for capture to $O^{2+}(2s2p^3\ ^1D^o)+He^+$ $(1s\ ^2S)$, $O^{2+}(2s2p^3\ ^3D^o)+He^+$ $(1s\ ^2S)$, and $O^{2+}(2s2p^3\ ^3P^o)+He^+$ $(1s\ ^2S)$ increase with increasing collision energy, which may be due to the weak radial coupling at short internuclear distances, while the cross section for capture to $O^{2+}(2s2p^3\ ^1P^o)+He^+$ $(1s\ ^2S)$ almost remains constant over the considered energy region.

Looking at the state-selective cross sections in detail, some oscillatory structures are found in the energy range from 1 to 100 eV/u for both $^2\Sigma^+$ and $^2\Pi$ states, as shown in Fig. 8. The obvious oscillations in the $O^{2+}(2s2p^3\ ^3P^o)+He^+$ $(1s\ ^2S)$ channel in the $^2\Sigma^+$ and $^2\Pi$ symmetries are due to its interference with the $O^{2+}(2s2p^3\ ^3D^o)+He^+$ $(1s\ ^2S)$ channel,

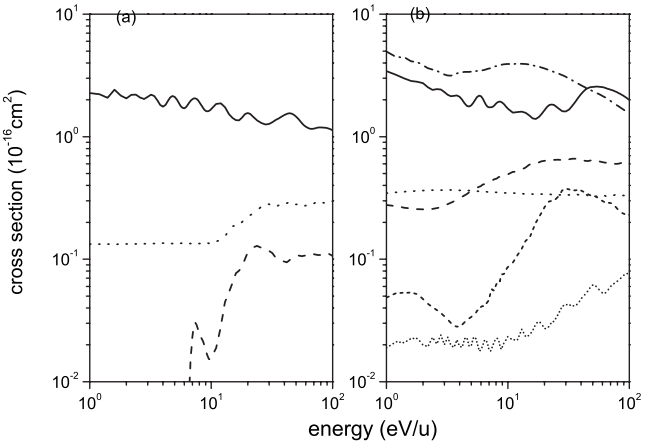

FIG. 8. Oscillations in the state-selective charge-transfer cross sections for O^{3+}+He. (a) State-selective cross section for $^2\Sigma^+$ channels; (b) state-selective cross section for $^2\Pi$ channels. Solid line: electron captured to $[O^{2+}(2s2p^3\ ^3P^o)+He^+(1s\ ^2S)]$; dashed line: $[O^+(2s^22p^3\ ^2P^o)+He^{2+}]$; dotted line: $[O^{2+}(2s2p^3\ ^1P^o)+He^+(1s\ ^2S)]$; dash-dotted line: $[O^{2+}(2s2p^3\ ^3P^o)+He^+(1s\ ^2S)]$; short-dashed line: $[O^+(2s^22p^3\ ^2D^o)+He^{2+}]$; short-dotted: $[O^{2+}(2s2p^3\ ^1D^o)+He^+(1s\ ^2S)]$.

since the charge-transfer cross sections for these two channels are comparable in magnitude. The interferences between the $O^{2+}(2s^22p^3\ ^2D^o)+He^{2+}$ and $O^{2+}(2s2p^3\ ^1D^o)+He^+$ $(1s\ ^2S)$ channels and between the $O^+(2s^22p^3\ ^2P^o)+He^{2+}$ and the $O^{2+}(2s2p^3\ ^1P^o)+He^+$ $(1s\ ^2S)$ channels also produce some oscillations.

Experimentally, Bangsgaard *et al.* [12] have only reported some state-selective cross-section data at a few collision energies (see Table III of Ref. [12]). Due to limitations in re-

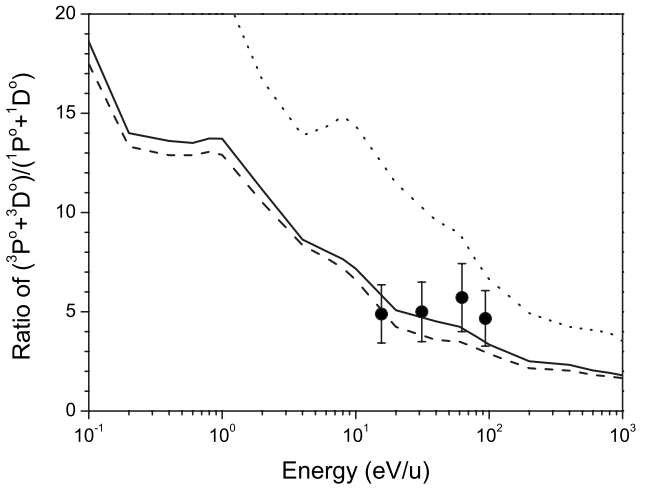

FIG. 9. The state-selective SEC cross-section ratios for capture to the triplet states $O^{2+}(2s2p^3\ ^3P^o, ^3D^o)$ and singlet states $O^{2+}(2s2p^3\ ^1P^o, ^1D^o)$. Solid line: the present QMOCC results with the contribution of DEC $^2P^o$ included in the $^1P^o+^1D^o$ cross section; dashed line: present QMOCC results with the contributions of DEC $^2P^o$ and $^2D^o$ included in $^1P^o+^1D^o$ cross section; dotted line: present QMOCC results without the contributions of DEC included in $^1P^o+^1D^o$ cross section; filled circles: results of the experiment of Bangsgaard *et al.* [12].

solving power in the translational energy-gain spectra experiment, the product channels cannot be assigned separately and thus the experimental results were given as the summation over channels with similar energy defects. For comparison, the cross-section ratio of $(^3P^o+^3D^o)/(^1P^o+^1D^o)$ is computed and shown in Fig. 9 with the results of Ref. [12]. In the current calculation, the DEC cross sections to the $^2P^o$ and $^2D^o$ channels are included for the $^1P^o$ and $^1D^o$ states of similar energy defects and the value of their ratio is shown as a dashed line in Fig. 9, while the results with the $^2D^o$ cross sections added to the $^1P^o$ and $^1D^o$ are represented as a solid line. The present calculations agree with the measurements of Bangsgaard *et al.* [12] within the experimental error, which further confirms the accuracy of the present QMOCC and MRDCI calculations. For 500 eV incident energy (31.25 eV/u), the calculated cross-section ratio of $^3P^o/^3D^o$ is about 0.97, which is consistent with the energy-gain spectrum of Bangsgaard *et al.* (see Fig. 3 of Ref. [12]) and thus would appear to resolve the previous conflict between measurement and calculation [12]. Over the whole energy region considered, capture to the $^3P^o$ and $^3D^o$ channels is dominant, while the importance of other channels increases increasing incident energy. The contributions of $^3P^o$ and $^3D^o$ and that from other channels become comparable when the collision energy is larger than 10 eV/u. Also shown in Fig. 9 is the pure SEC triplet-singlet ratio which is seen to be greater than the statistical value of 3 at all considered energies, but approaches the statistical value at the highest energy.

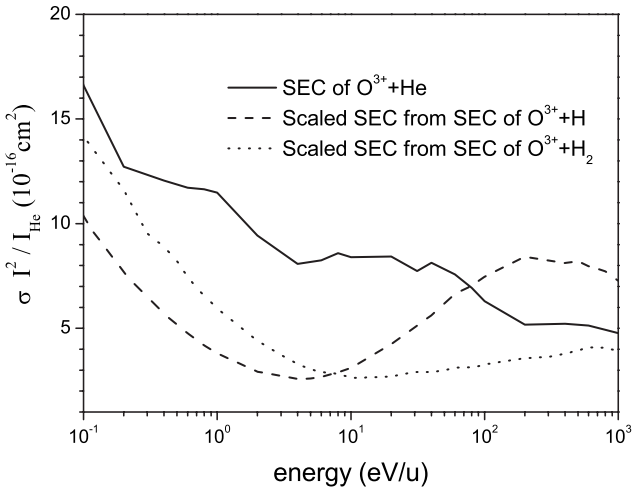

FIG. 10. Total SEC cross sections for O^{3+}+He collisions. Solid line: the present QMOCC results; dashed line: the scaled SEC cross sections from the QMOCC SEC of O^{3+}+H [31]; dotted line: the scaled SEC cross sections from the QMOCC SEC of O^{3+}+H_2 [31]. Noted that the I in *Y* axis represents the ionization potential of H and H_2, respectively.

In Fig. 10, we compare the total SEC cross section for O^{3+}+He with SEC cross sections for H and H_2 also obtained with the QMOCC method [31]. Here we have scaled the cross sections by the square of the target ionization potentials as suggested by the COB model for collision systems with

TABLE III. Total SEC and state-selective charge-transfer rate coefficients (cm^3/s) as a function of temperature. Note that the number in square brackets indicates the power of 10.

T (K)	Total	$^3D^o(2s2p^3)$	$^3P^o(2s2p^3)$	$^2D^o(2s^22p^3)$	$^1D^o(2s2p^3)$	$^2P^o(2s^22p^3)$	$^1P^o(2s2p^3)$
100	6.82[−10]	1.32[−10]	5.35[−10]	1.15[−12]	1.33[−12]	7.57[−12]	6.10[−12]
200	7.15[−10]	1.19[−10]	5.76[−10]	1.34[−12]	1.42[−12]	8.50[−12]	8.65[−12]
400	7.33[−10]	1.07[−10]	5.99[−10]	1.68[−12]	1.50[−12]	1.11[−11]	1.27[−11]
600	7.45[−10]	1.05[−10]	6.07[−10]	1.93[−12]	1.55[−12]	1.34[−11]	1.59[−11]
800	7.61[−10]	1.12[−10]	6.12[−10]	2.14[−12]	1.60[−12]	1.54[−11]	1.86[−11]
1000	7.82[−10]	1.23[−10]	6.17[−10]	2.32[−12]	1.64[−12]	1.71[−11]	2.10[−11]
2000	9.11[−10]	2.07[−10]	6.45[−10]	3.06[−12]	1.85[−12]	2.30[−11]	3.05[−11]
4000	1.14[−9]	3.63[−10]	6.60[−10]	4.32[−12]	2.18[−12]	2.97[−11]	4.44[−11]
6000	1.31[−9]	4.68[−10]	7.46[−10]	5.31[−12]	2.49[−12]	3.44[−11]	5.54[−11]
8000	1.44[−9]	5.41[−10]	7.86[−10]	6.02[−12]	2.78[−12]	3.88[−11]	6.47[−11]
10000	1.54[−9]	5.96[−10]	8.21[−10]	6.55[−12]	3.06[−12]	4.33[−11]	7.29[−11]
20000	1.95[−9]	7.94[−10]	9.65[−10]	9.28[−12]	4.25[−12]	6.88[−11]	1.04[−10]
40000	2.59[−9]	1.11[−9]	1.18[−9]	2.22[−11]	6.39[−12]	1.27[−10]	1.50[−10]
60000	3.12[−9]	1.35[−9]	1.35[−9]	4.33[−11]	8.57[−12]	1.86[−10]	1.88[−10]
80000	3.58[−9]	1.53[−9]	1.51[−9]	6.73[−11]	1.09[−11]	2.40[−10]	2.24[−10]
100000	3.97[−9]	1.66[−9]	1.67[−9]	9.10[−11]	1.34[−11]	2.88[−10]	2.56[−10]
200000	5.39[−9]	1.98[−9]	2.36[−9]	1.78[−10]	2.68[−11]	4.63[−10]	3.89[−10]
400000	6.87[−9]	2.12[−9]	3.19[−9]	2.56[−10]	5.06[−11]	6.71[−10]	5.78[−10]
600000	7.72[−9]	2.12[−9]	3.70[−9]	2.98[−10]	6.79[−11]	8.18[−10]	7.28[−10]
800000	8.39[−9]	2.08[−9]	4.10[−9]	3.31[−10]	8.12[−11]	9.39[−10]	8.62[−10]
1000000	8.99[−9]	2.03[−9]	4.47[−9]	3.59[−10]	9.20[−11]	1.05[−9]	9.86[−10]

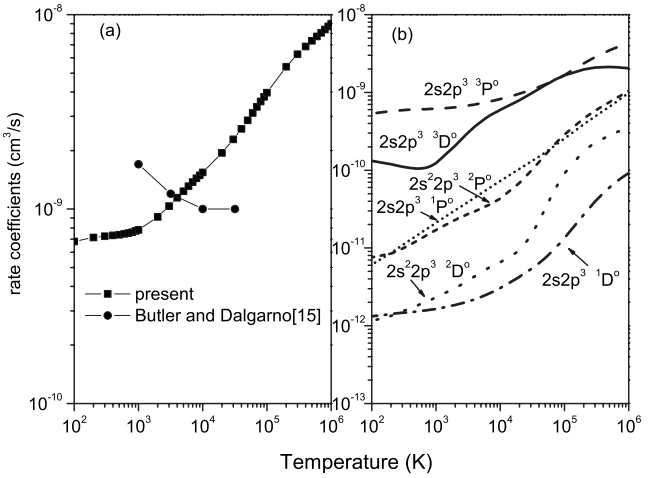

FIG. 11. Total SEC and state-selective rate coefficients in charge transfer of $O^{3+}(^2P^o)$ with He as a function of temperature. (a) Total rate coefficients: solid line with filled squares: present results; solid line with filled circles: results of Butler and Dalgarno [15]; (b) present QMOCC state-selective rate coefficients.

the same initial charge. As expected, the cross sections for the different targets are very different being sensitive to the molecular structure of the quasimolecules. At the highest energies the total SEC cross sections begin to become comparable, but still display a factor of 2–3 discrepancy at 1 keV/u. As noted in many other studies, the COB model should be used with caution.

C. Total and state-selective rate coefficients

Total SEC and state-selective charge-transfer rate coefficients were calculated using the cross sections obtained by the QMOCC method and are plotted in Fig. 11. The only previous calculation was that of Butler and Dalgarno [15] who used a two-channel LZ method, but for a limited temperature range. The agreement is fair given the approximations adopted in Ref. [15] for this complex system. It can be found from Fig. 11(b) that the single-electron charge-transfer processes for capture to the $O^{2+}(2s2p^3\ ^3P^o)$ and $O^{2+}(2s2p^3\ ^3D^o)$ dominate over the other channels for the whole temperature range considered. The double-electron charge-transfer process becomes significant with increasing temperature with capture to the $O^{+}(2s^22p^3\ ^2P^o)$ becoming comparable to that for the $O^{2+}(2s2p^3\ ^3P^o)$ and $O^{2+}(2s2p^3\ ^3D^o)$ at $T=10^6$ K. The total SEC and state-selective rate coefficients are also tabulated in Table III.

V. SUMMARY

Charge-transfer processes due to collisions of ground-state $O^{3+}(2s^22p\ ^2P)$ ions with atomic helium are investigated using the QMOCC method. The *ab initio* adiabatic potential and radial coupling utilized in the QMOCC calculations are obtained from the MRD-CI approach. Total cross section and especially the state-selective cross section of the electron capture processes are provided for collision energies from 0.01 eV/u to 1 keV/u. Comparison with existing data shows that the present QMOCC calculations agree quite well with the experimental results for total and state-selective single-electron capture cross sections. Further theoretical and experimental studies are needed to explore noted discrepancies in double capture processes.

ACKNOWLEDGMENTS

This work was partly supported by the National Natural Science Foundation of China (Grants No. 10604011, No. 10734140, No. 10008803, and No. 10878008) and the National Key Laboratory of Computational Physics Foundation (Grant No. 9140C6904030808). P.C.S. acknowledges NASA Grant No. NNG05GD98G.

[1] S. Lepp and R. McCray, Astrophys. J. **269**, 560 (1983).
[2] S. I. Krasheninnikov, A. Yu. Pigarov and D. J. Sigmar, Phys. Lett. A **214**, 285 (1996); A. Yu. Pigarov and S. I. Krasheninnikov, *ibid.* **222**, 251 (1996).
[3] R. K. Janev, T. Kato, and J. G. Wang, Phys. Plasmas **7**, 4364 (2000).
[4] A. Owens, A. N. Parmar, T. Oosterbroek *et al.*, Astrophys. J. **493**, L47 (1998).
[5] C. M. Lisse *et al.*, Science **274**, 205 (1996).
[6] M. J. Mumma, V. A. Krasnopolsky, and M. J. Abbott, Astrophys. J. **491**, L125 (1997).
[7] T. E. Cravens, Geophys. Res. Lett. **24**, 105 (1997).
[8] R. M. Häberli, T. I. Gombosi, D. L. De Zeeuw *et al.*, Science **276**, 939 (1997).
[9] D. Bodewits *et al.*, Astron. Astrophys. **469**, 1183 (2007).
[10] T. E. Cravens, E. Howell, J. H. Waite, Jr. *et al.*, J. Geophys. Res., [Space Phys.] **100**, 17153 (1995).
[11] V. Kharchenko, A. Dalgarno, D. R. Schultz, and P. C. Stancil, Geophys. Res. Lett. **33**, L11105 (2006).
[12] J. P. Bangsgaard, P. Hvelplund, J. O. P. Pedersen, L. R. Andersson, and A. Barany, Phys. Scr., T **T28**, 91 (1989).
[13] K. Ishii, A. Itoh, and K. Okuno, Phys. Rev. A **70**, 042716 (2004).
[14] E. Y. Kamber, O. Abu-Haija, and J. A. Wardwell, Phys. Rev. A **77**, 012701 (2008).
[15] S. E. Butler and A. Dalgarno, Astrophys. J. **241**, 838 (1980).
[16] R. J. Buenker, and S. D. Peyerimhoff, Theor. Chim. Acta **35**, 33 (1974); **39**, 217 (1975); R. J. Buenker, Int. J. Quantum Chem. **29**, 435 (1986).
[17] R. J. Buenker, in *Proceedings of the Workshop on Quantum Chemistry and Molecular Physics, Wollongong, Australia*, edited by P. G. Burton (Wollongong University Press, Wollongong, Australia, 1980); *Study in Physical and Theoretical Chemistry*, Current Aspects of Quantum Chemistry Vol. 21 (Elsevier, Amsterdam, 1981), p. 17; R. J. Buenker and R. A. Phillips, J. Mol. Struct.: THEOCHEM **123**, 291 (1985).

[18] S. Krebs and R. J. Buenker, J. Chem. Phys. **103**, 5613 (1995).
[19] D. E. Woon and T. H. Dunning, Jr., J. Chem. Phys. **100**, 2975 (1994).
[20] T. H. Dunning, Jr., J. Chem. Phys. **90**, 1007 (1989).
[21] http://physics.nist.gov/cgi-bin/ASD/energy1.pl; W. L. Wiese, J. R. Fuhr, and T. M. Deters, J. Phys. Chem. Ref. Data Monogr. **7** (1996); G. W. F. Drake and W. C. Martin, Can. J. Phys. **76**, 679 (1998).
[22] B. Herrero, I. L. Cooper, and A. S. Dickinson, J. Phys. B **29**, 5583 (1996).
[23] G. Hirsch, P. J. Bruna, R. J. Buenker, and S. D. Peyerimhoff, Chem. Phys. **45**, 335 (1980).
[24] M. Kimura and N. F. Lane, Adv. At., Mol., Opt. Phys. **26**, 79 (1990).
[25] B. Zygelman, D. L. Cooper, M. J. Ford, A. Dalgarno, J. Gerratt, and M. Raimondi, Phys. Rev. A **46**, 3846 (1992).
[26] J. G. Wang, P. C. Stancil, A. R. Turner, and D. L. Cooper, Phys. Rev. A **67**, 012710 (2003); **69**, 062702 (2004).
[27] B. R. Johnson, J. Comput. Phys. **13**, 445 (1973).
[28] T. G. Heil, S. E. Butler, and A. Dalgarno, Phys. Rev. A **27**, 2365 (1983).
[29] D. L. Cooper, N. J. Clarke, P. C. Stancil, and B. Zygelman, Adv. Quantum Chem. **40**, 37 (2001).
[30] B. H. Brandsen and M. R. C. McDowell, *Charge Exchange and the Theory of Ion-Atom Collisions* (Clarendon Press, Oxford, 1992).
[31] A. R. Turner, D. L. Cooper, J. G. Wang, and P. C. Stancil, Phys. Rev. A **68**, 012704 (2003).
[32] P. C. Stancil *et al.*, J. Phys. B **34**, 2481 (2001).
[33] J. G. Wang *et al.*, J. Phys. B **35**, 3137 (2002).
[34] R. K. Janev, L. P. Presnyakov, and V. P. Shevelko, *Physics of Highly Charged Ions* (Springer-Verlag, New York, 1985).
[35] L. F. Errea, C. Harel, H. Jouin, L. Méndez, B. Pons, and A. Riera, J. Phys. B **27**, 3603 (1994).
[36] E. H. Nielsen, L. H. Andersen, A. Barany, H. Cederquist, J. Heinemeier, P. Hvelplund, H. Knudsen, K. B. MacAdam, and J. Ssrensen, J. Phys. B **18**, 1789 (1985).